LIMNOLOGY
and
OCEANOGRAPHY: METHODS

Limnol. Oceanogr.: Methods 11, 2013, 511–528

Hyperspectral imaging of the microscale distribution and dynamics of microphytobenthos in intertidal sediments

Arjun Chennu[1], Paul Färber[1], Nils Volkenborn[2,3], Mohammad A. A. Al-Najjar[1,4], Felix Janssen[1,5], Dirk de Beer[1], and Lubos Polerecky[1,6*]*

[1]Max Planck Institute for Marine Microbiology, Celsiusstr. 1, Bremen 28359, Germany
[2]Dept. of Biological Sciences, University of South Carolina, Columbia SC 29208, USA
[3]IFREMER, Laboratory of Benthic Ecology, Technopole Brest BP70, Plouzane, France
[4]Red Sea Research Center, King Abdullah University of Science and Technology, Jeddah, Saudi Arabia
[5]Alfred Wegener Institute for Polar and Marine Research, Am Handelshafen 12, 27570 Bremerhaven,Germany
[6]Department of Earth Sciences, Utrecht University, Budapestlaan 4, 3584 CD Utrecht, The Netherlands

Abstract

We describe a novel, field-deployable hyperspectral imaging system, called Hypersub, that allows noninvasive in situ mapping of the microphytobenthos (MPB) biomass distribution with a high spatial (sub-millimeter) and temporal (minutes) resolution over areas of 1 × 1 m. The biomass is derived from a log-transformed and near-infrared corrected reflectance hyperspectral index, which exhibits a linear relationship ($R^2 > 0.97$) with the chlorophyll *a* (Chl *a*) concentration in the euphotic zone of the sediment and depends on the sediment grain size. Deployments of the system revealed that due to factors such as sediment topography, bioturbation, and grazing, the distribution of MPB in intertidal sediments is remarkably heterogeneous, with Chl *a* concentrations varying laterally by up to 400% of the average value over a distance of 1 cm. Furthermore, due to tidal cycling and diel light variability, MPB concentrations in the top 1 mm of sediments are very dynamic, changing by 40-80% over a few hours due to vertical migration. We argue that the high-resolution hyperspectral imaging method overcomes the inadequate resolution of traditional methods based on sedimentary Chl *a* extraction, and thus helps improve our understanding of the processes that control benthic primary production in coastal sediments.

Microphytobenthos (MPB), consisting of benthic phototrophs such as microalgae, cyanobacteria, and dinoflagellates, is the fundament of the trophic food web in coastal ecosystems. In shallow-water environments, such as intertidal flats and estuaries, MPB represents a considerable portion of the autotrophic biomass, accounting for up to 50% of the primary production (MacIntyre et al. 1996; Nozais et al. 2001; Spilmont et al. 2006). MPB is the predominant food source for many deposit-feeding organisms, and the activity and distribution of MPB profoundly affect nutrient fluxes across the sediment-water interface, sediment geochemistry, as well as sediment morphology and stability (Sundbäck et al. 1991; Montagna et al. 1995; Miller et al. 1996; Stal 2010).

The spatio-temporal organization of a community is a prominent issue in ecology. Levin (1992) argued that analysis of large-scale (regional) patterns must integrate effects occurring at smaller scales. Generally, the distribution of MPB is affected by both abiotic processes (e.g., nutrient availability, hydrodynamic exposure, sediment type) and biotic processes (e.g., grazing, competition) through a complex network of interactions. In their reductionist approach to benthic ecology, Miller et al. (1996) argued that studies of interactions with a direct effect on the MPB distribution (so called "isolated first-order interactions") are required to disentangle the complex relationships between the sediment bed, infaunal organisms, and the water column, and for a comprehensive picture

*Corresponding authors: E-mails: achennu@mpi-bremen.de; l.polerecky@uu.nl

Acknowledgments

We thank the laboratory technicians of the Microsensor group and the electronic and mechanical workshops at the Max Planck Institute for Marine Microbiology for their invaluable assistance throughout the implementation of this project. We also thank Justus van Beusekom, Karsten Reise, and Elisabeth Herre from the Alfred Wegener Institute for Polar and Marine Research, and George Matsui, Sarah Woodin, and David Wethey from the University of South Carolina for their support during field campaigns. This work was funded by the Marie Curie Initial Training Network "SENSEnet" (grant nr 237868), the National Science Foundation (OCE 0928002), and the Max Planck Society of Germany.

DOI 10.4319/lom.2013.11.511

of shallow-water ecosystems to emerge. The small scale of perception (which relates to the body size) and short generation times of the organisms are thought to lead to a high degree of spatio-temporal variability for MPB (Azovsky et al. 2004), and several studies emphasized the importance of gathering quantitative data on MPB distributions at a sub-millimeter scale (Underwood et al. 2000; Seuront and Spilmont 2002; Murphy et al. 2008), which is in the range of perception of the MPB organisms. However, most previous work was generally unable to resolve the spatial variability in MPB distributions below the decimeter range (5-10 cm) (Moreno and Niell 2004; Seuront and Leterme 2006; Spilmont et al. 2011).

MPB biomass is considered a basic environmental descriptor in benthic studies (Bale and Kenny 2007), and is estimated through the measurement of Chl *a* concentrations in surficial sediments. This is typically done by collecting sediment cores from the field site and measuring absorbance or autofluorescence of Chl *a* extracted from the sediment using a solvent (Lorenzen 1967; Whitney and Darley 1979). This procedure, although time-consuming and labor-intensive, has been widely used to estimate the spatial structure and temporal dynamics of MPB biomass (Guarini and Blanchard 1998; Brito et al. 2009b; Spilmont et al. 2011). A troubling feature of this method has been the lack of standardization of the protocol involved, such as sampling core diameter, sampling depth, the number of replicates, or the extraction solvent, which makes it challenging to compare results of different studies (Grinham et al. 2007; Brito et al. 2009a). A further disadvantage of the method is that it is destructive and does not allow repetitive measurements at the same location.

Recently, optical methods have been explored as alternatives to extractive methods for Chl *a* quantification in sediments. They provide the potential to measure rapidly enough to capture the MPB biomass distribution within the relevant spatial (mm) and temporal (min) scale, and have the additional advantage of being essentially non-invasive (reviewed by Kühl and Polerecky 2008).

One approach of optical Chl *a* quantification in sediments is based on the measurement of in vivo auto-fluorescence. Although this approach offers high sensitivity and high signal-to-noise ratio (Serôdio et al. 1997), it is encumbered by practical difficulties such as the requirement of dark (or low-light) adaptation of the measured MPB community (Honeywill et al. 2002; Jesus et al. 2005, 2006).

An alternative approach for optical Chl *a* quantification in sediments is reflectance spectrometry, which is based on the measurement of light back-scattered from the sediment at wavelengths around 675 nm, i.e., the wavelength of maximal in vivo Chl *a* absorption (Hakvoort et al. 1997). One implementation of this approach uses a spectrometer with hyperspectral resolution to collect light back-scattered from several square centimeters of the sediments surface (Kromkamp et al. 2006; Forster and Jesus 2006). Although successfully applied in the field, the fact that this approach is essentially a single-point measurement makes it impractical for achieving a sub-millimeter spatial resolution across larger areas. To improve the spatial resolution, Murphy et al. (2004, 2009) used color-infrared cameras for the detection of back-scattered light in three wavelength bands, including near-infrared light. Although this imaging approach decreased the spatial resolution to about 0.5 mm, the lack of spectral resolution is an impediment to the spectrometric analysis of the sediment reflectance, which undergoes subtle variations depending on the sediment type or the MPB composition, and may therefore influence the interpretation of results (Kazemipour et al. 2011; Barillé et al. 2011).

The capture of back-scattered light with simultaneously high spatial and spectral resolution has been enabled by using hyperspectral cameras. As shown by Polerecky et al. (2009a), this approach can be used for pigment identification, localization, and relative quantification on scales ranging from single cells to whole microbial communities. This versatility is achieved by simply changing the optical arrangement (i.e., microscope versus different types of lenses) in front of the camera. This system greatly facilitated studies on the structure and composition of benthic photosynthetic microbial communities such as microbial mats (Bachar et al. 2008; Kohls et al. 2010; Al-Najjar et al. 2012), biofilms (Kühl and Polerecky 2008; Polerecky et al. 2009b; Ionescu et al. 2012) or modern stromatolites (Farías et al. 2013). However, hyperspectral imaging at a high (sub-millimeter) spatial resolution has so far been limited to laboratory-based measurements across relatively small areas (few squared centimeters).

This study describes a novel hyperspectral imaging system for in situ quantification of pigments in benthic ecosystems. The system, called Hypersub, is an adaptation of the system developed by Polerecky et al. (2009a), and enables field-based, remotely operable, and underwater spectral reflectance measurements with sub-millimeter resolution over areas of about one squared-meter. The hyperspectral resolution (~ 1 nm) enables a variety of spectrometric analyses, including the quantification of the concentration of Chl *a* and other photopigments in sediments. We used artificial biofilms for the calibration and validation of the system against a well-established method based on pigment extraction and spectrophotometry. We then used Hypersub to study the spatio-temporal variations of Chl *a* in surficial sediments of intertidal sandflats, such as those associated with sediment topography, sediment bioturbation, and vertical migration of MPB linked to tidal and diel light cycles.

Materials and procedures

Hardware components

The primary components of the submersible hyperspectral imaging system Hypersub are two imagers, imaging optics, and control electronics, all enclosed in an underwater housing mounted on a mechanical sledge (Fig. 1A-B). Additional components include a pair of halogen lamps (BLV Whitestar 5000-6500 K) for supplementary illumination, a motorized sledge for mov-

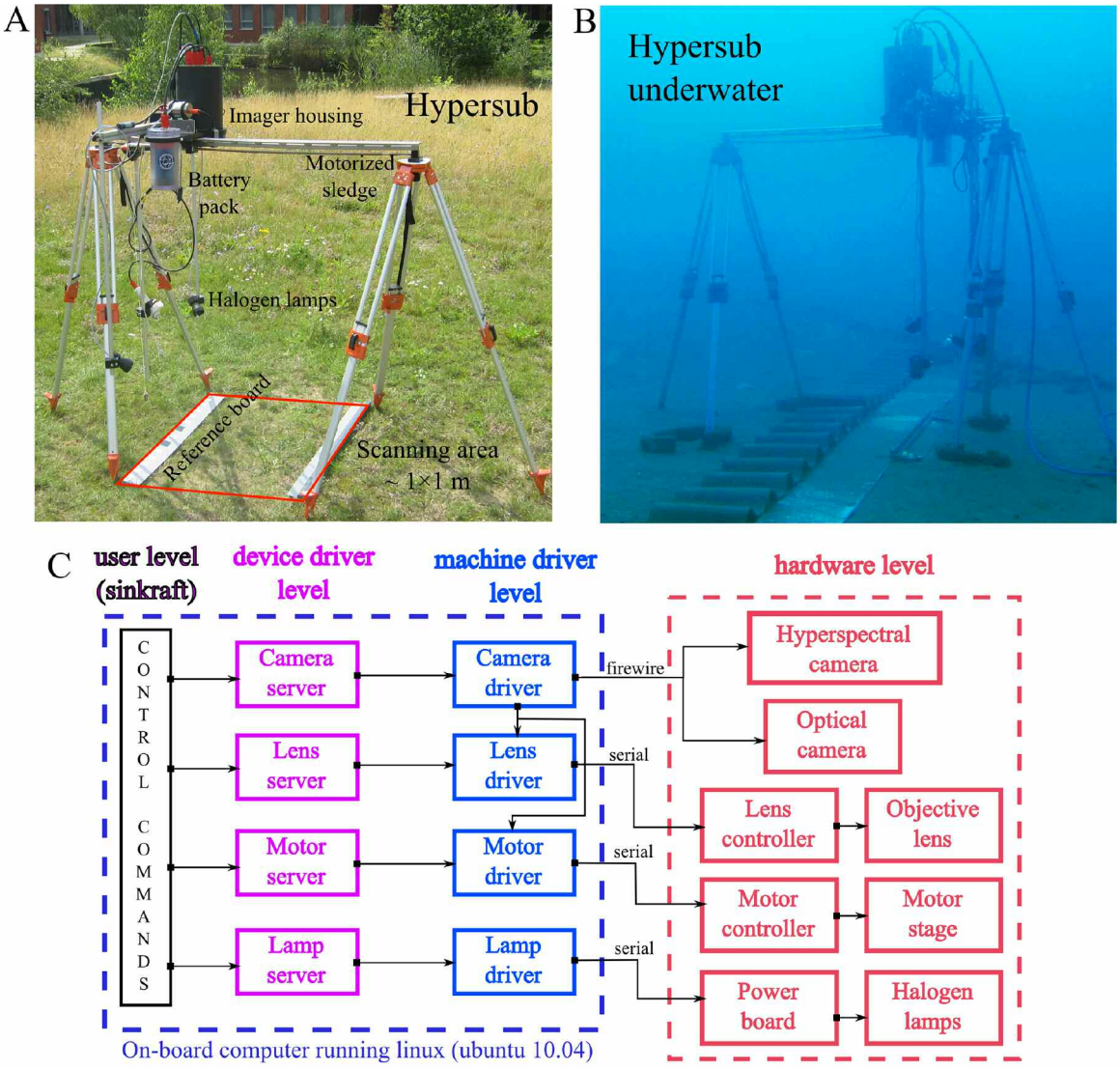

Fig. 1. Photographs of Hypersub, the novel submersible hyperspectral imaging system, showing the primary components mounted on a motorized sledge. A schematic diagram of the hardware and software architecture of the system is shown in panel C.

ing the cameras across the imaged area, and an on-board battery pack. The mechanical sledge is driven along a threaded stainless-steel rail by a motor that can also be used underwater, and allows scanning across a distance of 1 m at a maximal velocity of about 3 mm s^{-1}. Combined with the view of the imaging optics, the maximum size of the scanning area is about 1 × 1 m.

The first imager, a hyperspectral camera (PIKA-II; Resonon Inc.), is used to resolve and capture back-reflected light in 480 spectral bands (bandwidth of ~ 1 nm) across the range of wavelengths from blue (400 nm) to near-infrared (900 nm). The imager is a line camera that directs incoming light from each spectral band onto a measuring line of 640 pixels, which can be considered as the "line of view." The second imager (Guppy; Allied Vision Technologies GmbH) is a standard monochrome camera and is used to record the scanned region as gray-scale images of visible light intensity. Both imagers provide a firewire port (IEEE 1394) as the electronic interface to the control system, which is also used to transfer the acquired image data to a storage device. These components are sealed inside an underwater housing (rated to a depth of 75 m) with an optical window (PMMA) that transmits across the spectral range of the imagers. Once the underwater housing is sealed, the necessary adjustments to the zoom, aperture, and focus of the objective lenses (Fujinon Inc. or Pentax Inc.) are done via a custom-built electronic control circuit.

The control electronics comprises a single-board computer (PC/104; Kontron AG), which runs a Linux operating system (Ubuntu 10.04) and provides interfaces for firewire, ethernet, and serial communication. The firewire ports are used to control image acquisition, the serial ports are used to control the motor, lenses, and the halogen lamps, and the ethernet port allows for network operations (Fig. 1C).

The battery pack for Hypersub consists of three rechargeable lithium-polymer cells (12 V 16 Ah; Headway Headquarters LLC; 40160SE). This supports an active measurement time of 3-4 h (including illumination by the halogen lamps). Because one scan typically requires about 10 min, this allows for acquisition of about 15-20 hyperspectral scans. With the use of timer-circuits, all devices can be powered off between measurements, which allows extension of the overall deployment time to about 1 week. The electronics housing also contains a circuit that can draw electricity from an external power source and recharge the on-board battery pack, allowing for extended field deployments. Effectively, Hypersub can be operated with the only external dependencies being a 12-24 V recharging power supply and an ethernet connection for communication.

Measurement software

A custom-built software (Sinkraft), which runs on the Hypersub computer, establishes a network platform for the various devices to communicate and interact. Sinkraft is written in Python (www.python.org) and makes use of several free software libraries. It follows a modular design that reflects the modular design of the hardware (Fig. 1C). Each device is associated with a TCP server that provides a communication interface with clients (e.g., another device or a user within the local network) to perform device-specific operations. This enables real-time remote operations at the device-level, as well as autonomous operation through text scripts that embody a measurement protocol (see Table 1).

While measuring, the frames acquired from the imagers are sequentially stored in a 16-bit binary file on the storage disk. Additionally, the binary file is accompanied by a meta-data file that contains information about the data file structure, wavelengths, time of measurement and motor positions for each frame. Formatting of both files complies with common hyperspectral imaging standards (see http://geol.hu/data/online_help/ENVI_Header_Format.html).

Measurement procedure

A hyperspectral scan is performed by mounting the imagers facing the object (e.g., sediment surface), and acquiring image frames as the sledge is moved along the rail (Fig. 1A). Before acquiring images, several optical adjustments have to be performed. First a region-of-interest is selected using an interactive viewer of the line-of-view and field-of-view seen by the hyperspectral and direct imagers, respectively. Optionally, the halogen lamps can be switched on if the ambient illumination is insufficient. Subsequently, the exposure is adjusted to ensure optimal dynamic range of the detected light intensity across the entire spectral range of sensitivity, which is done by adjusting the shutter duration of the imagers and the aperture size of the objectives. Finally, the focus of the objectives is

Table 1. An example of a protocol script for conducting a hyperspectral scan with the *Sinkraft* software used in Hypersub.

Sinkraft commands*	Actions performed†
@manager act start @ipower; @ipower set ports 1; @self sleep 2;	# start the power module to power other devices and wait 2 s for hardware initialization
@manager act start @hscam @hslens @optcam @optlens @motor @lamps @timer;	# now start all other devices
@motor set lims –20 1010; act abspos !! 0;	# set motor scanning limits in mm. Then, move motor to start (0) position; wait until arrival (!!)
@lamps set ports 1;	# switch on lamps
@hscam set fps 7.5; @optcam set fps 15;	# set frame-rates of hs-imager and gray-scale imager
@hscam act autoexpose; act autofocus; @optcam act autoexpose; act autofocus;	# perform auto-exposure and auto-focusing with imagers
@hscam set scan $name = hsi $filename = hs_scan $logmotor = @motor; @optcam set scan $name = vis $triggertime = 10 $filename = vis_scan $logmotor = @motor;	# define scan parameters for both imagers. Files are sequentially numbered on repetition
@optcam act startscan vis; @self pause 0.1; @hscam act startscan hsi; @self pause 0.1;	# start frame acquisition by both imagers
@motor act relmm !! 1000;	# move motor by 1000 mm, blocking further execution of the script until the distance has been traversed
@hscam act stopscan hsi; @optcam act stopscan vis;	# stop frame acquisition after motor movement
@lamps set ports 0; @motor act abspos !! 0;	# scanning completed. Switch off lamps and move to start position before power off
@timer set reltimealarm 121; @manager act stop all; act systemhalt 60;	# set a wake-alarm to restart the system after 121 min, and execute power-off after 60 s

*The various devices/subsystems of Hypersub are referenced through device tokens such as @hscam, @optcam, @motor, etc. Semicolon is used for separation of commands.

†The # character marks the beginning of text used for documentation.

adjusted to optimize sharpness of a spatial feature (artificially introduced, if not present) seen by the cameras.

An important step during optical adjustments is to include a spectral reference board along the top or bottom edge of the imaged area (Fig. 1A). The pixels recorded as the hyperspectral imager scans across the reference board are used in subsequent data processing (see *Hyperspectral data analysis*) to calculate the spectral reflectance from the captured intensities of the back-scattered light. In principle the reference board can be made of any diffusely reflecting material with a flat reflectance spectrum in the wavelength region 400-900 nm, even if its reflectance is lower than 100%. In this study, we used white or gray plastic (PVC), which were checked against a reflectance standard (DLC DL-0510) to have a flat reflectance spectrum in the range 400-900 nm. The reference boards were prepared with a matte surface finish to eliminate specular reflection.

After the initial optical adjustments, the acquisition scan is initiated by a command to the motor to move the sledge at a constant velocity, and simultaneously, by a command to the imagers to acquire and record frames at a predefined frame-rate (typically 4 fps). During the scan, the position of the motorized sledge is recorded along with the time-stamp of each frame to allow accurate spatial reconstruction of the scanned area. To improve the signal-to-noise ratio of the acquired images, averaging of frames, or binning of spectral bands can be optionally applied. An example of the protocol scripts used in this study is shown in Table 1.

Hyperspectral data analysis

Hyperspectral measurements generate a rich multi-dimensional dataset, and require special software for processing and analysis. Based on previous ideas on hyperspectral analysis (Polerecky et al. 2009a), a custom analysis software was developed using Python. The software, called HyPurveyor, provides an interactive view of the hyperspectral data in both its spatial and spectral dimensions, and can be used to create contextual maps of arbitrary, user-defined spectral indices. Additionally, tools for spatial context analysis or image analysis are also available. All data presented in this study were analyzed using HyPurveyor.

Spectral-index for quantification of benthic Chl *a*

A typical reflectance spectrum of sediment covered with a microphytobenthic biofilm contains a pronounced valley at around λ_{max} = 675 nm due to in vivo absorption maximum of Chl *a*, and an approximately linear trend in the near-infrared (NIR) region due to the combined effects of absorption and scattering by the sediment-seawater matrix (Fig. 2; see also Murphy et al. 2005; Barillé et al. 2011). To account for these specific features, we calculated a hyperspectral microphytobenthos index (MPBI) as

$$\mathrm{MPBI} = \log[R_p] - \log[R_{\lambda max}] \quad (1)$$

where $R_{\lambda max}$ is the measured reflectance at λ_{max}, and R_p is the value of the fitted linear trend in the NIR range (720-800 nm) extrapolated to λ_{max} (Fig. 2). By using the extrapolated value R_p, the index effectively incorporates a form of "continuum correction" that is used to remove the effects of the sediment substrate on the overall shape of the reflectance spectrum (Clark and Roush 1984; Kokaly and Clark 1999). Furthermore, by incorporating logarithmic transformation of the reflectance ratio $R_p/R_{\lambda max}$, the index accounts for the exponentially decreasing light intensity within an MPB biofilm, which results in a linear relationship between the MPBI and Chl *a* concentrations in the biofilms (see *Assessment*), as opposed to the saturated exponential relationship found for spectral indices that are not log-transformed (Carrère et al. 2004; Barillé et al. 2011).

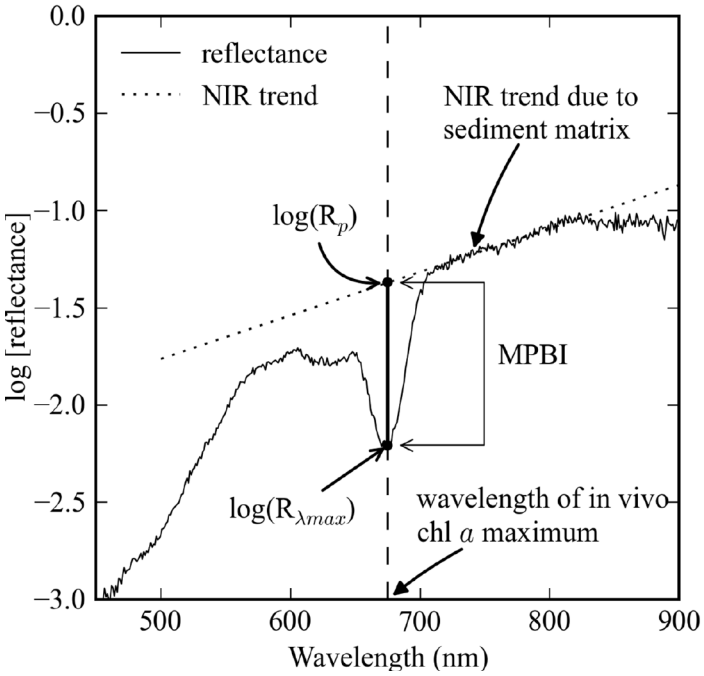

Fig. 2. A typical example of reflectance spectrum of intertidal sediment with a MPB biofilm, with a graphical representation of the spectrometric index (MPBI) used for the quantification of the MPB biomass in terms of the sedimentary Chl *a* concentration.

Using HyPurveyor, the calculation of MPBI was done in each pixel of the spatial image. To minimize the influence of the sensor noise, the $R_{\lambda max}$ value was calculated from the fit of the reflectance spectrum around λ_{max} by a third-order polynomial rather than from the reflectance measured in a single band. By implementing a calibration, the hyperspectral MPBI values were then converted to Chl *a* concentrations and displayed as color-coded images.

Preparation of artificial biofilms for calibration and validation

Calibration and validation of the hyperspectral imaging system for Chl *a* quantification in sediments were done using artificial biofilms prepared by mixing natural sediment grains with diatoms from a laboratory culture. Sediments were col-

lected from various intertidal sites in the North Sea and sorted by sieving into 4 grain-size groups: < 63 μm, 63-125 μm, 125-250 μm, and 250-355 μm. These groups roughly represent muddy (0-125 μm) and sandy (125-355 μm) sediments. The sorted sediment grains were then boiled with hydrogen peroxide (90%) at 65°C to remove any dissolved organic content and dried again in an oven at 80°C. Concentrated diatom suspensions (species *Amphora Coffeaeformis*) were prepared by centrifugation of the diatom culture in the exponential growth phase. Subsequently, the suspensions were added to the sediment at various concentrations and mixed with a low-gelling agar (1.5% wt.) at temperature of 40°C. While still fluid, the mixture was cast into plastic molds (20 × 10 × 1 mm) and left to cool for about a minute, resulting in 1-mm-thick solidified sediment biofilms. Additionally, reference "biofilms" with no added diatoms were also prepared. The biofilm thickness of 1 mm was chosen to match the typical penetration depth of light in natural marine sediments (see *Discussion*).

Scanning of the calibration and validation biofilms took around 10-15 min and was done while the biofilms were submersed in seawater. Because the solidified agar prevented diatom migration, the initially homogeneous diatom distribution in the biofilms was maintained homogeneous throughout the measurements. Immediately after scanning, the biofilms were subjected to 90% acetone, sonicated for 2 min in tubes, and placed at –20°C overnight to extract the intracellular Chl *a*. For each tube, the absorption spectrum of the filtered extractant was measured (USB4000; Ocean Optics Inc.) and the Chl *a* concentration therein was calculated based on spectrophotometric comparison with a standard (C5753; Sigma-Aldrich Co.). This value was subsequently multiplied by the known volume of the extractant to obtain the Chl *a* content in the biofilm.

Quantification of benthic Chl *a*

Chlorophyll *a* contents in the calibration and validation biofilms were normalized to the biofilm's porewater volume. Consequently, all Chl *a* concentrations in this study are reported in "micrograms of Chl *a* per milliliter of porewater" (μg Chl *a* mL^{-1} PW). This choice of normalization, although not used in benthic studies, better reflects the fact that it is the porewater where the MPB cells reside, interact with light, and thus contribute to primary productivity. Additionally, it has an advantage that it allows a more straightforward comparison between the concentrations of photosynthetically active biomass in pelagic and benthic ecosystems (the pelagic Chl *a* concentrations are typically reported per liter of water). In benthic studies, sedimentary Chl *a* concentrations are typically reported in units normalized to sediment weight (μg Chl *a* per g of wet or dry sediment weight) or to sediment area (μg Chl *a* per m^2 of sediment). The conversion between our volume-normalized Chl *a* concentrations and those normalized to the sediment weight or area is straight-forward: [μg Chl *a* g^{-1} dry wt.] = [μg Chl *a* mL^{-1} PW] × (φ/ρ_{DS}), [μg Chl *a* g^{-1} wet wt.] = [μg Chl *a* mL^{-1} PW] × $\varphi/(\rho_{DS} + \varphi \times \rho_{PW})$, and [mg Chl *a* m^{-2}] = [μg Chl *a* mL^{-1} PW] × φ × d, where φ is the sediment porosity, ρ_{DS} is the bulk density of dry sediment (g mL^{-1}), ρ_{PW} is the porewater density (g mL^{-1}), and d (in mm) is the depth range for which the areal Chl *a* concentration is reported (d = 1 mm in this study). To achieve brevity, the following text will omit "Chl *a*" and "dry wt." in the units of Chl *a* concentrations, with "g" always referring to sediment dry weight.

Assessment

Calibration and validation of the method using artificial biofilms

To calibrate the hyperspectral method, artificial MPB biofilms with variable but spatially homogeneous Chl *a* concentrations were scanned with Hypersub and the MPBI values obtained for each sample (using Eq. 1) were averaged over all measured pixels. The values were subsequently corrected for an offset, $MPBI_0$, measured in biofilms prepared from the same sediments but with no diatoms added, and plotted against the porewater volume-specific Chl *a* concentrations determined through extraction.

The relationship between the Chl *a* concentrations and the offset-corrected MPBI values was very well ($R^2 > 0.97$) described by a linear model

$$\mathrm{chl}a\left[\mu\mathrm{g\ ml^{-1}PW}\right] = S \times \left(\mathrm{MPBI} - \mathrm{MPBI}_0\right) \qquad (2)$$

Linearity was maintained for Chl *a* concentrations from 4 to 820 μg mL^{-1} PW, with a lower accuracy below 10 μg mL^{-1} PW and no systematic deviations toward the upper end of concentrations (Fig. 3A). Assuming sediment porosity of 0.4, the range of linear response corresponds to 0.016 – 3.3 × 10^5 mg m^{-3} of sediment volume. Thus, the system is able to quantify MPB biomass over a wide range of concentrations that are typically found in natural MPB biofilms (0.03 – 7 × 10^5 mg m^{-3}; Krause-Jensen and Sand-Jensen 1998).

An important finding of the calibration step is that the sensitivity (or slope) of the calibration, *S*, as well as the zero-chlorophyll offset, $MPBI_0$, depend strongly on the sediment grain-size (Table 2; Fig. 3B). This is, most likely, due to the close coupling between the geometrical characteristics of the sediment (grain-size and packing) and its light-scattering properties (see *Discussion*). The fact that the $MPBI_0$ offset is non-zero indicates that the linear continuum correction in the MPBI calculation did not fully account for the effect of the sediment matrix on the reflectance spectrum. The reason for this is unclear, but could be due to the slightly non-linear absorption of the agar-solidified sediment matrix in the wavelength range of 675-800 nm.

For the studied sediment type (silicate intertidal sediment), empirical functions that describe the dependencies of the calibration sensitivity, *S*, and of the offset, $MPBI_0$, on the grain-size are given in Fig. 3B. Using these functions, one can estimate a potential error that can be made if the prediction of the

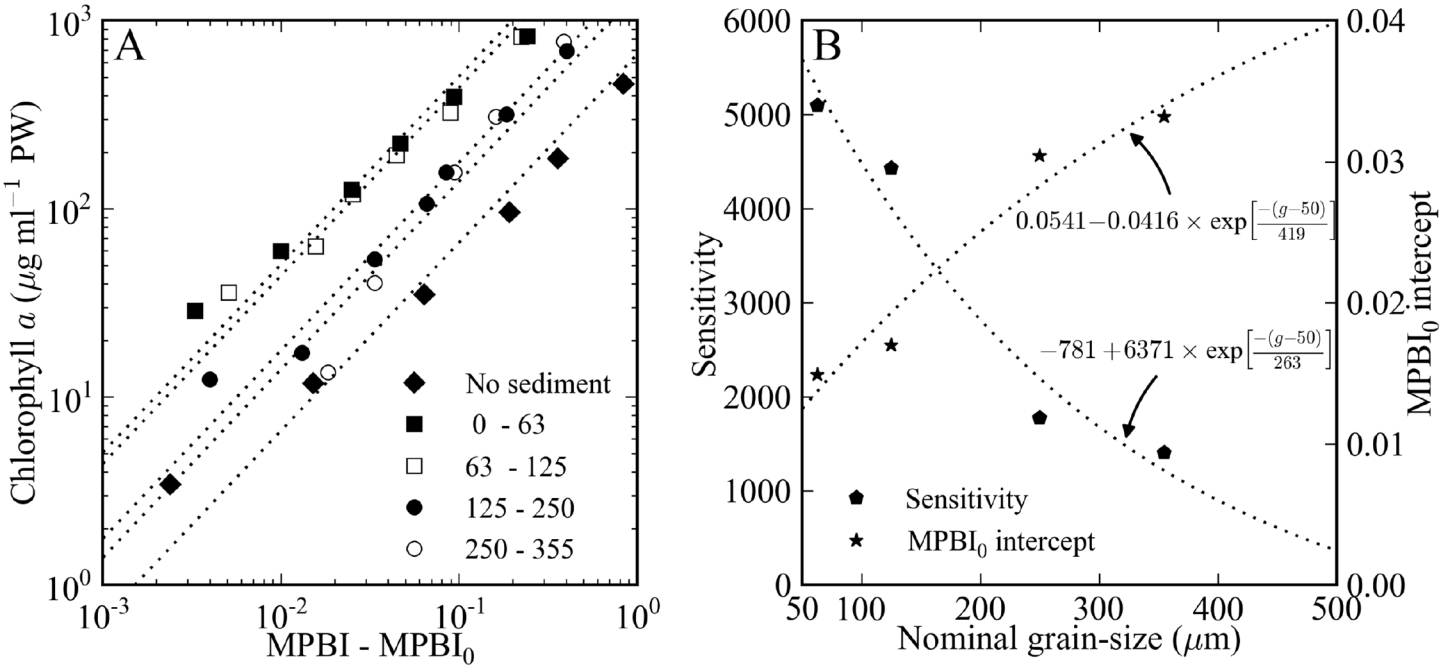

Fig. 3. Calibration plots (panel A) of the hyperspectral microphytobenthic index (MPBI) versus the concentration of Chl *a* in artificially prepared mixtures of MPB and sediment. Dotted lines show least-square fits with a line given by Eq. 1. The values of the parameters S and $MPBI_0$ for the studied sediment types (see legend) are given in Table 1 and depend on the nominal grain-size as shown in panel B.

Table 2. Parameters of calibration between the hyperspectral microphytobenthic index, MPBI, and porewater Chl *a* concentrations (Eq. 1).

Nominal grain-size (micrometer)	Sensitivity S (μg Chl *a* mL^{-1} PW)	$MPBI_0$ Intercept	Correlation coeff. (R^2)
0	665	0.002	0.9904
1–63	5094	0.015	0.9980
63–125	4432	0.017	0.9862
125–250	1776	0.030	0.9728
250–355	1407	0.033	0.9913

sedimentary Chl *a* concentration is done without reliable information about the sediment grain-size. For example, for an MPBI value of 0.1, the Chl *a* concentration predicted for a fine muddy sediment (grain sizes < 63 μm) would be 433 μg mL^{-1} PW, whereas it would be about 4-fold lower for a coarse sandy sediment (grain sizes 250-355 μm). This demonstrates that the knowledge of sediment characteristics is very important for accurate quantification of the Chl *a* concentration in sediments based on the measurement of spectral reflectance, in agreement with conclusions reached in previous studies (Murphy et al. 2005; Spilmont et al. 2011).

To validate the method and assess its predictive power, independent measurements were performed on a different set of biofilms prepared from the same sediment and diatoms, and the Chl *a* concentrations predicted from the measured MPBI were compared against those obtained through extraction. Both Chl *a* concentrations followed well a 1:1 line (Fig. 4A). However, Chl *a* values for some samples differed by up to ± 40% (on average by about ± 20%), and this difference varied depending on the grain-size of the sediment used (whiskers in Fig. 4B). This shows that even with careful biofilm preparation and measurements, Chl *a* concentrations obtained by the hyperspectral and extraction-based method may differ by several tens of percent, similar to results obtained by others (Carrère et al. 2004; Murphy et al. 2009). It is likely that this phenomenon is linked to the small differences in the size distribution and especially the compaction of grains in each prepared biofilm, which affect the hyperspectral signal by influencing the scattering properties of the sediment (see *Discussion*). This is consistent with the relatively strong dependence of the calibration parameters on the nominal grain-size (Fig. 3B), and further supported by the fact that calibration parameters derived for the "validation biofilms" differed by as much as 40% from those derived for the cali-

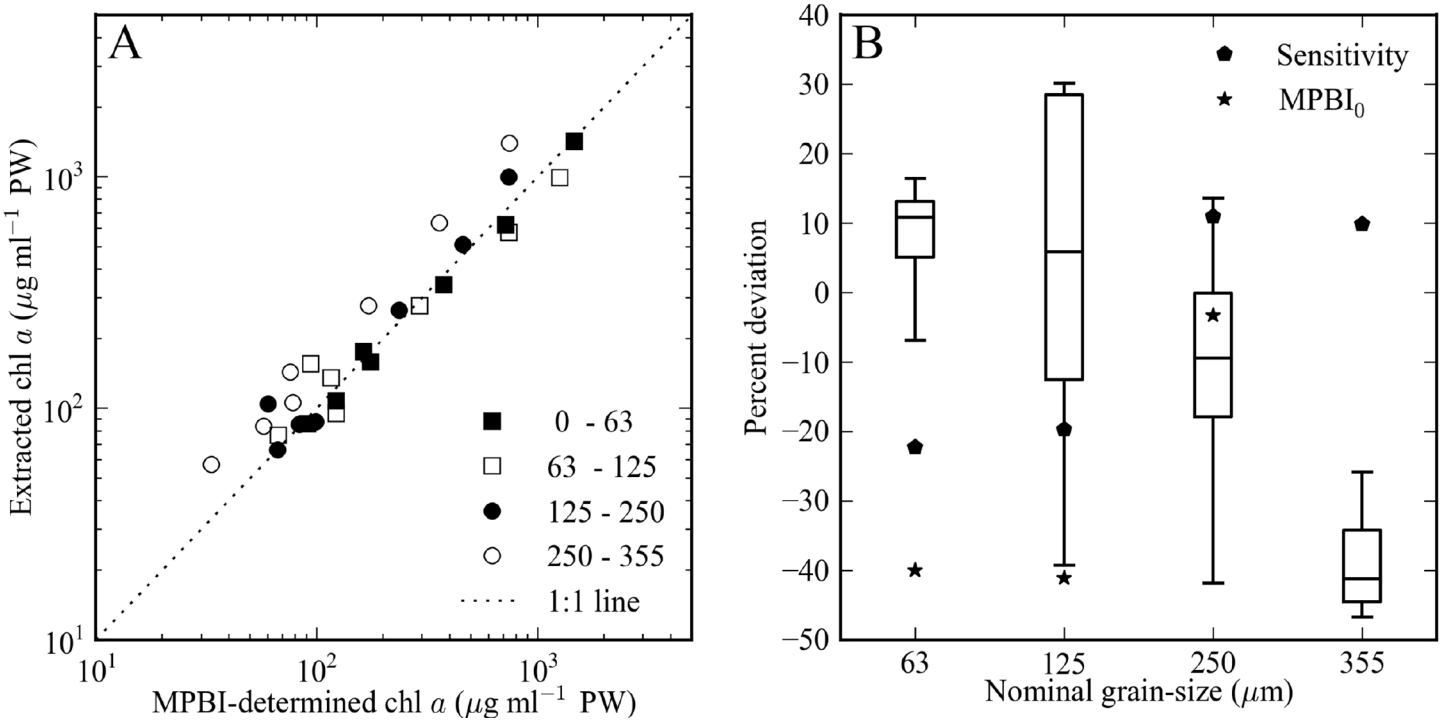

Fig. 4. Validation of the hyperspectral imaging method for Chl *a* quantification in MPB biofilms. (A) Chlorophyll *a* concentrations calculated from the measured MPBI using calibration parameters shown in Fig. 3 versus those measured via spectrophotometric analysis of extracted pigments. (B) The box-whisker plot shows percentage deviations between the calculated and measured Chl *a* concentrations, as derived from data shown in panel A, with boxes spanning the upper and lower quartiles, horizontal lines indicating the median, and whiskers extending to the full range of values. Filled symbols show the percentage deviation of the calibration parameters (S and MPBI0) determined from the independently prepared "validation" and "calibration" biofilms.

bration biofilms (see filled symbols in Fig. 4B), although both sets of biofilms were prepared from the same sediments and diatoms.

These relatively large discrepancies imply that the calibration shown in Table 2 and Fig. 3 cannot be applied universally for all sediments. Instead, both the slope *S* of the calibration line and the zero-chlorophyll offset $MPBI_0$ must be obtained individually for each studied sediment to allow accurate prediction of Chl *a* concentrations. Moreover, hyperspectral reflectance imaging should be accompanied by parallel measurements of the grain-size distribution if the latter characteristic of the studied sediment is expected to vary significantly within the imaged area.

Effects of vertical distribution of Chl *a*

The effects of a sub-millimeter scale vertical distribution of surficial Chl *a* on hyperspectral measurements were studied by imaging stacked biofilms. First, homogeneous biofilms were prepared similarly as for the calibration (see above) but with a thickness of 0.5 mm instead of 1 mm. The Chl *a* concentrations in these biofilms were in the ratio of 1:4. Subsequently, a biofilm with a higher Chl *a* concentration was placed on top of one with a lower Chl *a* concentration, or vice versa, resulting in 1 mm thick biofilms with a well-defined (two-layer) vertical distribution of Chl *a*. After imaging the stacked biofilms with Hypersub, the Chl *a* concentration in each 0.5 mm layer was separately quantified through extraction and spectrophotometry.

In general, MPBI values determined for stacked biofilms with a larger Chl *a* concentration on top ("high-low" biofilms) were larger than those with the reversed Chl *a* distribution ("low-high" biofilms), although the depth-integrated Chl *a* content in both biofilm types were similar (Fig. 5A). The difference depended on the grain size and ranged from 2-fold for the coarse-grained (125-250 μm) to about 3-fold for the fine-grained (<63 μm) sediment. This shows that the hyperspectral imaging method is sensitive not only to the amount of Chl *a* in a specific region of sediment where light penetrates, but also to its vertical distribution within that region. On the one hand, this is an important drawback of the hyperspectral imaging method, as it cannot distinguish whether an apparent lateral variability in a MPB distribution is due to a truly variable MPB biomass concentration or due to a lateral variability in its vertical distribution. On the other hand, this phenomenon can be advantageously used for monitoring changes in vertical Chl *a* distribution in time, such as those due to vertical migration of MPB in sediments.

To assess this possibility, we analyzed in detail the relationship between the offset-corrected MPBIs for stacked biofilms (denoted as M_{HL} and M_{LH} for the high-low and low-high

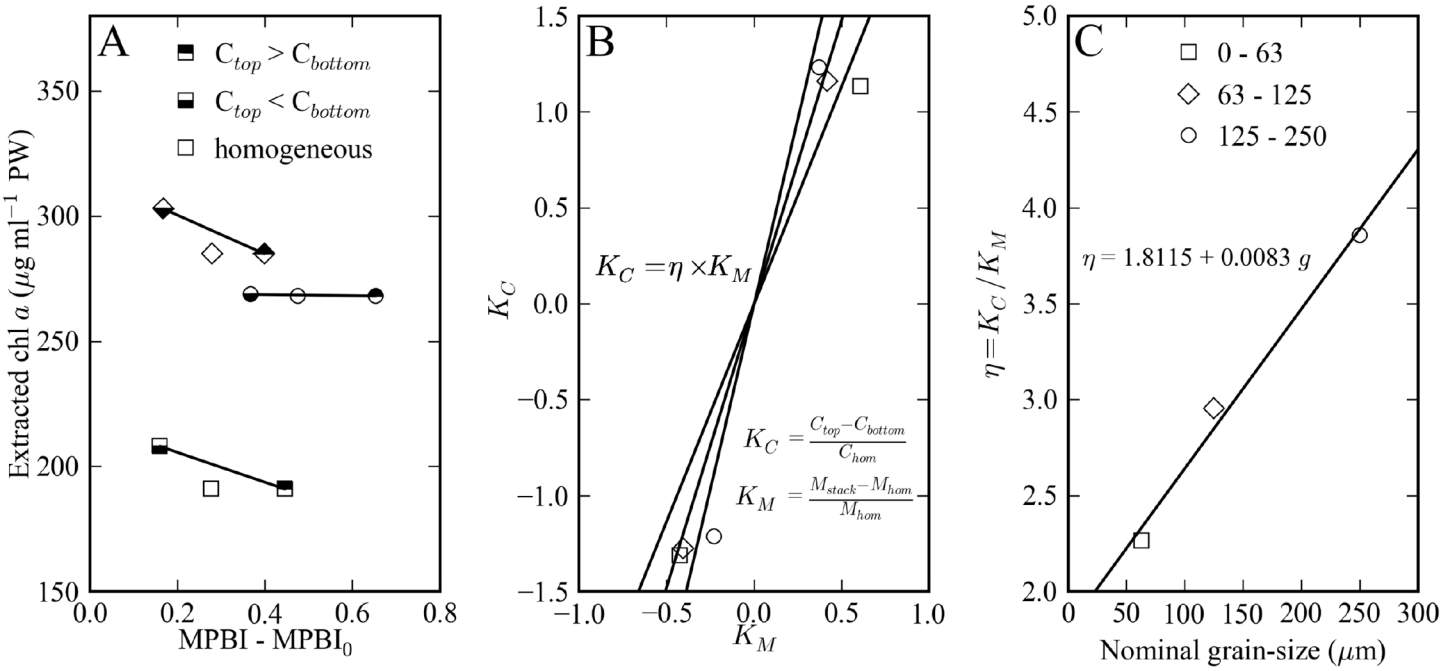

Fig. 5. The effect of the vertical distribution of chlorophyll a in a 1 mm thick MPB biofilm on the MPBI signal. (A) MPBI values for "high-low" and "low-high" stacked biofilms (half-filled symbols) and for homogeneous biofilms (unfilled symbols), plotted against the corresponding depth-integrated Chl *a* content in the biofilms. (B) Relationships between the MPBI contrast (KM, Eq. 3) and the chlorophyll contrast (KC, Eq. 4), as derived from data shown in panel A. (C) Slope of the relationship KC = η × KM as a function of the nominal sediment grain-size.

biofilms, respectively), the offset-corrected MPBIs for homogeneous biofilms with an equivalent depth-integrated Chl *a* amount in the top 1 mm (denoted as M_{hom}), the relative deviation of M from M_{hom}, defined as

$$K_M = \frac{M - M_{hom}}{M_{hom}} \quad (3)$$

and the contrasts in Chl *a* concentrations in the stacked biofilms, defined as

$$K_C = \frac{C_{top} - C_{bottom}}{C_{hom}} \quad (4)$$

where C_{top} and C_{bottom} are Chl *a* concentrations in the top and bottom half of the stacked biofilm, respectively, and $C_{hom} = (C_{top} + C_{bottom})/2$. We found that, irrespective of the grain-size, the MPB indices were with good accuracy related as $M_{hom} = (M_{HL} + M_{LH})/2$ (Fig. 5A). Furthermore, K_C depended on K_M by a linear relationship (Fig. 5B),

$$K_C = \eta \times K_M\ , \quad (5)$$

where the proportionality constant η depended on the nominal sediment grain-size *g* approximately linearly as η = 1.8115 + 0.0083*g* (Fig. 5C). Based on the definition, K_C represents the fraction of total Chl *a* in the 1 mm thick stacked biofilm that "moved" from the bottom half to the top half (or vice versa if $K_C < 0$) in comparison to the biofilm with a homogeneously distributed Chl *a* of equal total amount. Thus, assuming that the vertical Chl *a* distribution in natural MPB biofilms is approximated by a similar two-step function as in the stacked biofilms, Eqs. 3-5 allow estimation of the MPB fraction that vertically migrates within the top millimeter of the sediment from the measurement of temporal variations in MPBI (see section *Mapping of Chl* a *dynamics* below).

In situ microscale Chl *a* distribution

For the assessment of Hypersub in the field, we deployed it on an intertidal sandflat near the island of Sylt in the German North Sea (54.9°N, 8.3°E) and imaged "in situ" distributions of MPB on rippled and bioturbated sediments. Hyperspectral scans were performed using ambient sunlight, and spanned an area of approximately 80 × 20 cm in about 7-10 min. The obtained MPBI values were converted to Chl *a* concentrations in μg Chl *a* mL^{-1} PW assuming that the measured grain-size (125-250 μm) was constant across the imaged area (i.e., using the corresponding values for *S* and $MPBI_0$ given in Table 2). Additionally, using the measured sediment porosity (0.40), bulk density (1.55 g mL^{-1}), and the formula above, the values were also converted to μg g^{-1} to allow easier comparison with values available in the literature.

In the rippled sediment, the MPB distribution was remarkably variable, ranging from about 150 to 1620 μg mL^{-1} PW (38-418 μg g^{-1}) with a mean value of 710 μg mL^{-1} PW (183 μg g^{-1}), and clearly linked to the sediment topography (Fig. 6A-B). The gradients of Chl *a* concentrations were perpendicular to the

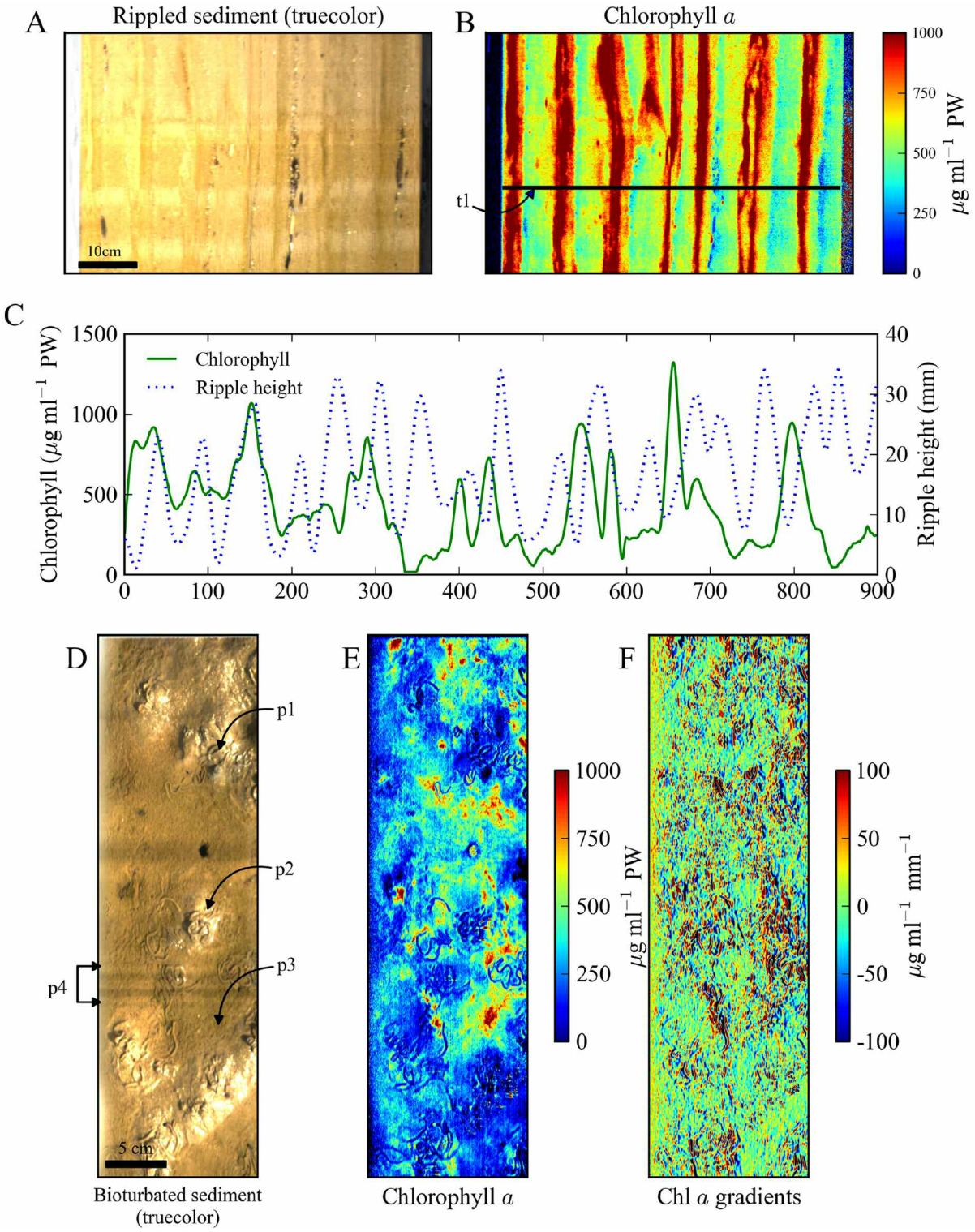

Fig. 6. In situ imaging of MPB biofilms on intertidal sediments using Hypersub. Shown are the true-color images and the corresponding Chl *a* maps of a rippled sea-bed (A, B) and of sediments affected by the bioturbation activity of lugworms *A. marina* (D, E). Features of the lugworm habitat such as fecal mounds (p1, p2) and inter-burrow sediment (p3) are annotated. Panel C shows an example of a lateral Chl *a* profile along a transect line t1 shown in B, overlaid with the corresponding profile of the ripple topography (height). Panel F shows 2D gradients of Chl *a* concentrations derived from the Chl *a* map in E. Note that due to the normalized nature of the MPBI calculation, the darker bands in panel D (p4), which are due to fluctuations in the illumination intensity during the scan caused by a passing cloud, are not visible in the Chl *a* map in panel E. Also note that the Chl *a* concentrations, given in µg mL^{-1} PW, can easily be converted to µg g^{-1} or mg m^{-2} using formulae given in *Materials and Procedures*.

ripple contour, and also remarkably steep, reaching up to 240 μg mL^{-1} PW mm^{-1} (62 μg g^{-1} mm^{-1}), which corresponds to a change of about 330% of the average Chl *a* concentration over a distance of 1 cm. A closer inspection of the Chl *a* concentration and the ripple height along randomly selected transects revealed that local minima in the MPB biomass were typically found on ripple troughs, while local maxima were located on ripple shoulders close to ripple crests (Fig. 6C). A possible explanation of this pattern could lie in the distribution of the shear force induced by the viscous drag of the water flow during the incoming and outgoing tide; during unidirectional tidal flow, the shear force would be highest on ripple crests, making it more difficult for MPB to accumulate there in high abundance, whereas the lowest shear stress would be at locations around the ripple shoulders (Bhaganagar and Hsu 2009).

The MPB distribution on the surface of sediments bioturbated by the lugworm *Arenicola marina* was also remarkably variable (20-1160 μg mL^{-1} PW or 5-300 μg g^{-1}), with an average around 300 μg mL^{-1} PW (77 μg g^{-1}). However, in contrast to the rippled sediment, the distribution was much more irregular (Fig. 6E). For example, the freshly defecated fecal mounds (p1, p2; Fig. 6D) had rather low Chl *a* concentrations, indicating efficient but not complete removal of the MPB cells by lugworm feeding. In contrast, sediments between the fecal mounds (p3; Fig. 6D) showed elevated Chl *a* concentrations, possibly indicating an enhanced growth rate of MPB, potentially due to an increased supply of nutrients from below driven by bioadvection (Chennu et al. in prep.), which is associated with the hydraulic activity of the lugworm (Rasmussen et al. 1998; Volkenborn et al. 2010). Spatial gradients of the MPB biomass in the bioturbated sediment were also remarkably high and comparable to those found for the rippled sediment. Maximal gradient values reached up to 250 μg mL^{-1} PW mm^{-1} (65 μg g^{-1} mm^{-1}), and more than 5% of pixel-locations had gradients above 110 μg mL^{-1} PW mm^{-1} (28 μg g^{-1} mm^{-1}) (Fig. 6F). The latter gradient corresponds to a change of about 400% of the average Chl *a* concentration over a distance of 1 cm, which highlights the profound microscale heterogeneity in the MPB distribution in bioturbated sediments.

In addition to the characterization of spatial patterns in sedimentary Chl *a* distributions, the high-resolution Chl *a* maps obtained by the Hypersub system can be used to assess sampling strategies for estimating the mean and variability of Chl *a* standing stocks in marine sediments. For this assessment, we used as an example the complete Chl *a* map obtained for the bioturbated sediment (Fig. 6E). This map contains 544000 measurements of Chl *a* concentrations over an area of 68 × 20 cm, and the true mean and standard deviation are M_t = 295 μg mL^{-1} PW and SD_t = 180 μg mL^{-1} PW, respectively, i.e., the coefficient of variation is $SD_t/M_t \times 100\% = 61\%$. The Chl *a* map was randomly sampled with N cores (N ranging from 5 to 500) of different diameters (ranging from 2 to 50 mm). This random sampling was repeated 500 times, and for each sampling the relative difference between the obtained mean, M_o, and the true mean, M_t, and between the obtained standard deviation, SD_o, and the true standard deviation, SD_t, was calculated as $|M_i\text{-}M_t|/M_t$ and $|SD_i\text{-}SD_t|/SD_t$, i = 1, 2,…, 500, respectively. Subsequently, the accuracy of the estimate was defined as the 95-percentile of these 500 relative deviations between the estimated and true values.

For a random sampling with N cores of 1 cm in diameter, the accuracy of the estimated mean decreased with N, reaching about 30% at n = 10 and 5% at n = 350 (Fig. 7). This means that the estimated mean by random sampling can differ by > 30% from the true mean when sampling with < 10 replicate cores, and only with > 350 randomly distributed cores, there is a > 95% certainty that the estimated mean deviates by < 5% from the true mean. The number of replicates required for a 5% accuracy of the estimated mean drops if the sampling is done with larger cores (e.g., n = 100 for the core diameter of 5 cm; Fig. 7). Clearly, this is because sampling with larger cores 'averages out' the small-scale variability that is detected when sampling with smaller cores. With respect to the variability of Chl *a* concentrations within the map, it was not possible to achieve < 5% difference between the estimated and true SD with 95% confidence even if the number of randomly sampled 1-cm diameter cores reached n = 500 (Fig. 7). This is clearly because the sampling core diameter was larger than the distance over which the Chl *a* distribution exhibited significant variations. Overall, this analysis demonstrates that sampling of a low number (5-10) of replicates is inadequate for accurate quantification of Chl *a* concentrations in highly heterogeneous systems such as bioturbated marine sediments. A similar conclusion was drawn in a recent study by Spilmont et al. (2011).

An interesting feature of the analysis of field data are that the 'shadow' regions in the true-color images, caused either by passing clouds or shadows of the frame of hypersub during the hyperspectral scan, are eliminated in the final Chl *a* maps (compare Figs. 6D and 6E, region p4). This is because the MPBI value is derived from the ratio of light intensities at essentially two wavelengths, one corresponding to the Chl *a* absorption maximum and the other in the NIR region where Chl *a* does not preferentially absorb (see Eq. 1 and Fig. 2). This approach provides an intrinsic correction against variations in incident light intensities within the dynamic range of the sensor during the scan, provided that during these variations the spectrum of the incident light remains unchanged.

Mapping of Chl *a* dynamics

To assess the suitability of the method for studying vertical migration of MPB, 3 round buckets (diameter 16 cm; depth 20 cm) were filled with freshly collected and sieved (0.5 cm mesh) surficial sediments from an intertidal flat near the Baruch Marine Field Laboratory in South Carolina (April; 33.3°N, 79.2°W), and incubated in a large tank with continuous flow-through of natural seawater. The sediments were inundated at all times and exposed to shaded natural light. Hyperspectral scans in about 1-2 h intervals were performed

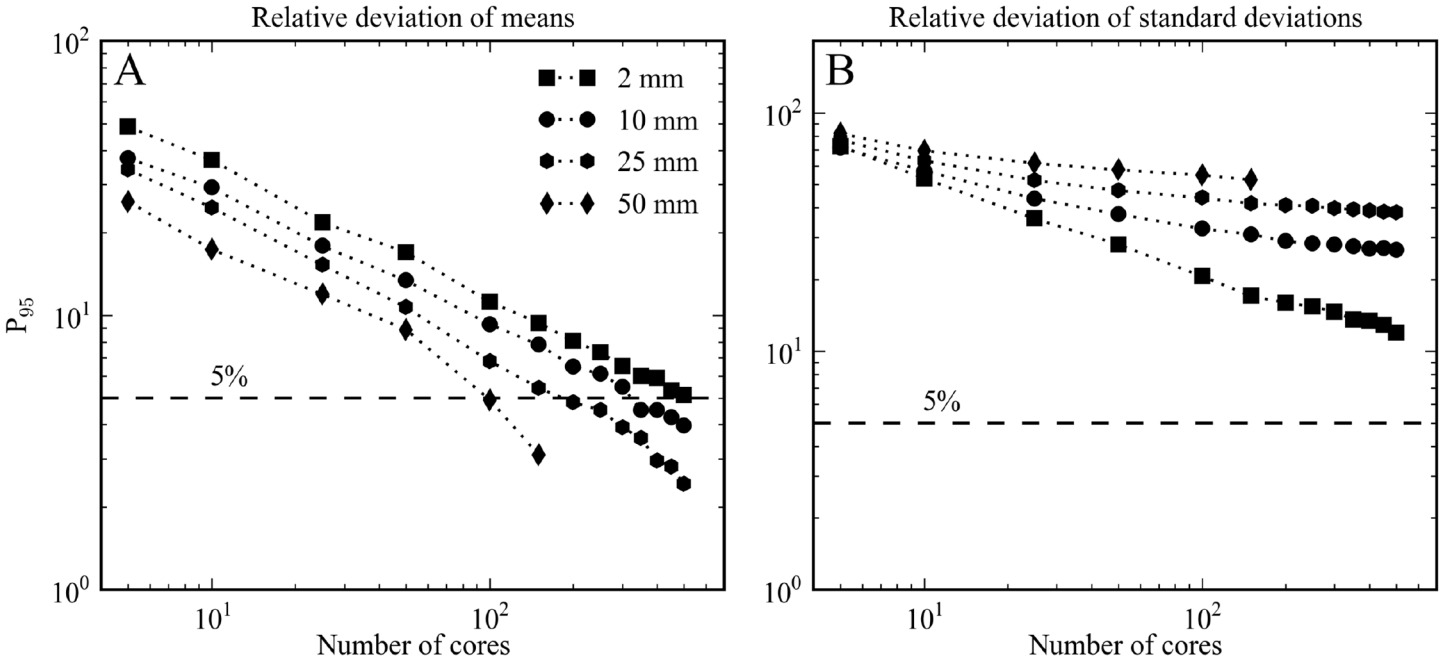

Fig. 7. Deviations between the true and estimated values of the mean (A) and the standard deviation (B) of Chl *a* concentrations in a bioturbated intertidal sediment. Shown are 95 percentiles derived from 500 random sampling attempts with N cores of different diameters (see legend), plotted as a function of the sample size N.

during daylight for 4 days and during the last night of the incubation. Overhead halogen lamps provided supplementary illumination during all scans. MPBI maps at the different time-points were aligned and analyzed with respect to spatial as well as temporal variability.

The MPBI values showed clear diel oscillations in every pixel of the sediment surface, with maximal values occurring shortly after midday and minimal values lasting from about 2 h after the sunset until shortly before sunrise (Fig. 8A). Based on the previous work on diel vertical migration of MPB (Palmer and Round 1967; Consalvey et al. 2004) and the fact that the amplitude of the MPBI oscillations as well as the maximal daily values did not change significantly during the measuring days, we assumed that the observed MPBI oscillations did not reflect changes in the total MPB biomass but were due to vertical migration of MPB.

To estimate the amount of migrating MPB, we used the daily MPBI minima and maxima observed in each pixel to calculate M_{hom} and the corresponding MPBI contrast K_M (Eq. 2). By assuming that the vertical Chl *a* distribution in the natural biofilms was well approximated by a two-layer model, we could use Eq. 4 to calculate the Chl *a* contrast K_C, which represents the fraction of the MPB that migrated daily within the top millimeter of the sediment. The migrating MPB fraction varied between 40% and 80% across the sediment surface (Fig. 6C), with the median averaged over the 3 replicate buckets of about 66%. A similar fraction of migrating MPB (40% to 50%) was obtained by direct cell counts in a previous study by Joint et al. (1982). Thus, although our measurements were indirect and based on several arguably crude approximations, they gave comparable results to those obtained by direct but considerably more labor-intensive measurements.

In addition to the mapping of the migrating MPB fraction, the non-invasive character of the hyperspectral imaging method also enabled mapping of the migration rate. To achieve this, the aligned MPBI images were subdivided into windows of 1 × 1 mm and the MPBI values averaged over these windows at time-points between the daily extrema were fitted as a function of time with a third-order polynomial. Subsequently, by combining Eqs. 3-5, the rate of MPB migration normalized to the total MPB content in the top 1 mm layer was calculated as

$$R_{migration} = \frac{dK_C}{dt} = \frac{\eta}{M_{hom}} \frac{dM(t)}{dt} \qquad (6)$$

This calculation revealed that the maximal rates of downward migration, observed shortly before the sunset, ranged from 2 to 12 % h^{-1} (average median of buckets about 7 % h^{-1}; Fig. 8D). That is, in the simplified two-layer approximation, 2% to 12% of the Chl *a* contained in the top 1 mm of the MPB biofilm migrated from the upper 0.5 mm to the lower 0.5 mm in 1 hour. The upward migration, observed shortly before the sunrise, was somewhat faster, ranging from about 4 to 14 % h^{-1} (median 9% h^{-1}; Fig. 8E). Furthermore, no spatial patterns were apparent in the migration rate maps (Fig. 8D-E), suggesting that MPB cells across the sediment surface in the buckets responded equally to the stimulus (incident light) that drives their vertical migration.

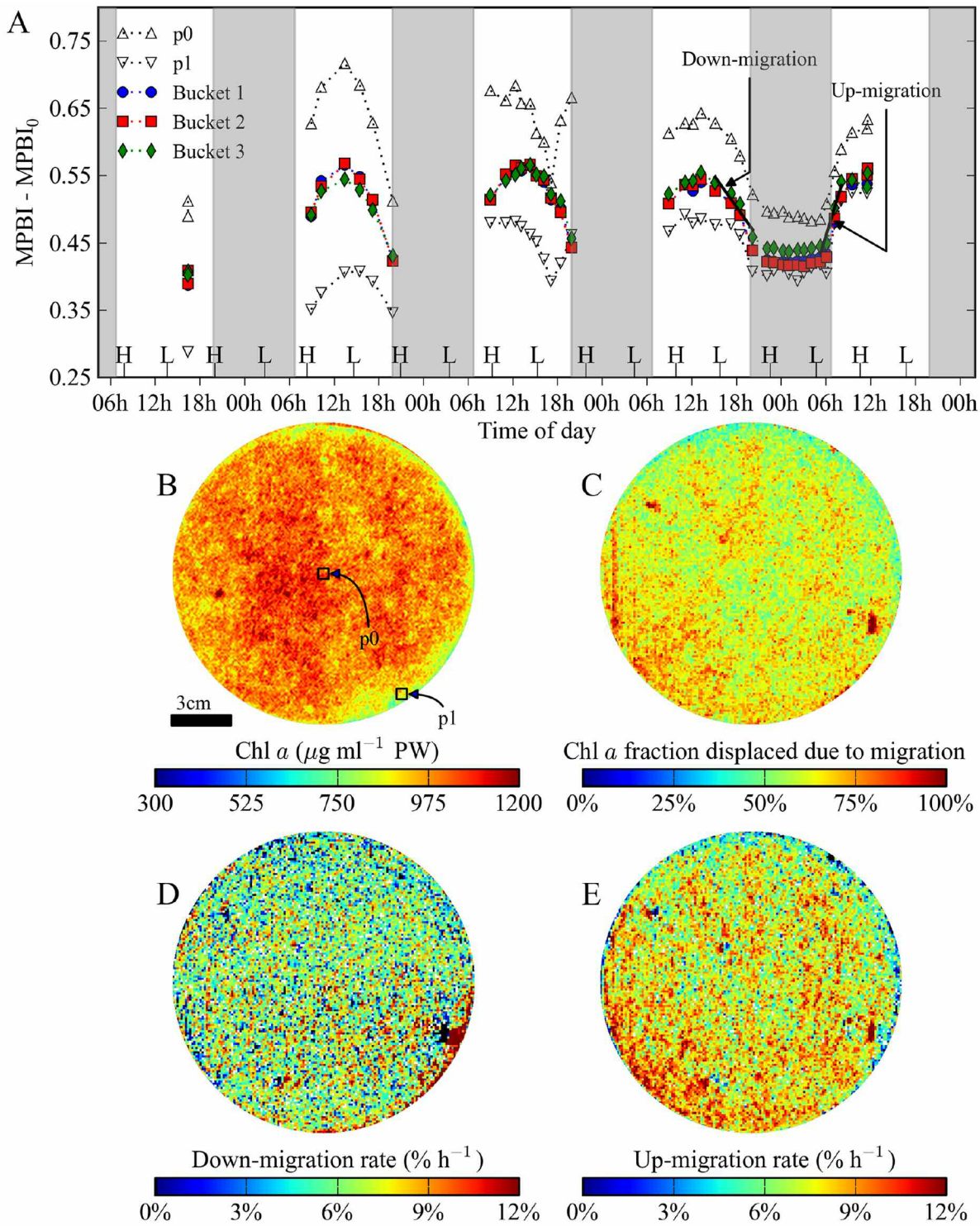

Fig. 8. Visualization of the spatio-temporal patterns in the distribution of Chl *a* in intertidal sediments associated with vertical migration of MPB. (A) MPBI index as a function of time over the course of 5 d, showing values in selected 5×5 mm areas (p0 and p1) and values averaged over the entire sediment surface in the experimental buckets. The gray and white areas correspond to nighttime and daytime, respectively, with the boundaries indicating the time of sunrise and sunset. Markers H and L indicate high and low tides, respectively. (B) Example of the Chl *a* distribution measured during midday. (C) Image of the fraction of MPB that migrated daily within the top millimeter of the sediment. (D-E) Images of the rates of downward (D) and upward (E) migration of MPB in the top millimeter of the sediment. The migrating fraction and rates are expressed in terms of a percentage of the Chl *a* standing stock in the top millimeter layer of the sediment. The rate maps provide a compact and quantitative visualization of the spatio-temporal dynamics of the chlorophyll distribution.

Discussion

Hypersub is a field instrument for quantification of Chl *a* in surficial sediments. The main attributes that make it an attractive tool for benthic studies are its spectral, spatial, and temporal resolutions, as well as the relatively large areas that can be imaged rapidly. For example, Chl *a* maps of about 1 m^2 with a lateral resolution of about 1 mm or better can be typically acquired in 5-10 min. The design of the system additionally allows underwater measurements (Fig. 1B), and this function is currently being tested and will be reported in greater detail elsewhere.

Chlorophyll *a* quantification is based on the measurement of spectral reflectance, derived from the detection of light back-scattered from the studied sediment surface. It is therefore minimally invasive and thus applicable for the study of spatio-temporal dynamics of Chl *a* distributions. The measurements can be performed under ambient natural illumination or, if not available, under artificial illumination from lamps that emit broadband light in the visible and near-infrared regions.

The instrument can be operated interactively or in a standalone automated mode, with the only external dependencies being a 12 V power supply (e.g., a battery or power line) and an ethernet connection. When powered solely by the built-in battery pack, the active measurement time is typically about 3-4 h, which is sufficient for the acquisition of about 15-20 hyperspectral scans. Through the implementation of a standby mode, these scans can be distributed over a total deployment time of about 1 week. The measurement control is done through a simple set of text-based commands, which are executed by the Sinkraft software on the Linux operating system that controls the onboard computer.

When quantifying the sedimentary Chl *a* concentrations from the measurement of spectral reflectance, an important question arises: what is the actual quantity that the measurement captures? A short answer to this question is that the reflectance measurement gives information about the concentration of Chl *a* in the sediment volume, specifically the interstitial porespaces that interact with the probing light and is therefore a measure of the biomass of MPB cells that contribute to benthic primary production through their photosynthetic activity. However, as shown by our investigations and discussed in the following, several issues need to be considered in this context.

First, the exact depth of probing cannot be easily estimated or generalized for different sediment types. According to the Beer-Lambert law, the intensity of light traveling through a scatter-free absorbing medium depends exponentially on the concentration of the absorbers, their absorbing strength (which usually strongly depends on the wavelength), and the effective optical path length. The problem is that in a complex media such as marine sediments, the effective optical path length is difficult to quantify as it is affected by absorption as well as by a high degree of multiple scattering on sediment grains, MPB cells, and other particles. The latter effect is especially important, as it can substantially prolong the effective path length of light within the sediment matrix, and thus influence the absorption imprint of the pigments present (Kühl and Jørgensen 1994; Yang and Miklavcic 2005). Since the scattering-induced path variations are generally unknown, it is methodologically impossible to determine two unknown entities—the true euphotic depth and the concentration of the absorbers (Chl *a*) within that depth—from a single reflectance measurement. Nevertheless, if the depth of optical probing is critical, it can be determined separately using light microprobes (Fenchel and Straarup 1971; Lassen et al. 1992). Previous measurements with this technique showed that although variable depending on factors such as the Chl *a* concentration, sediment grain-size, or wavelength, the light penetration depth in MPB biofilms is in the range 0.2–3 mm (Fenchel and Straarup 1971; Kühl et al. 1994; MacIntyre et al. 1996). Since 1 mm can be considered a reasonable intermediate light penetration depth in natural marine sediments, we used artificial biofilms of 1 mm thickness to conduct our calibration, validation, and stacked-biofilm measurements.

Second, the spectral reflectance-based method of Chl *a* quantification is sensitive not only to the amount of Chl *a* in the layer of sediment where the probing light penetrates, but also to its vertical distribution within that layer. When the vertical distribution is homogeneous, our calibration measurements showed that the relationship between the sedimentary Chl *a* concentration derived from traditional extraction-based spectrophotometric measurements and the microphytobenthic index (MPBI) derived from the spectral reflectance measurement is linear, with the sensitivity monotonously decreasing with the nominal sediment grain-size (Fig. 3). On the other hand, our measurements with stacked biofilms showed that MPBI can substantially change if the vertical Chl *a* distribution is not homogeneous (Fig. 5). More research is required to understand this relationship. With respect to natural sediments, epipelic diatoms such as *Amphora Coffeaeformis* form biofilms in the very top layers of the sediment surface (Mitbavkar and Anil 2004), whereas epipsammic species are more homogeneously distributed in the top centimeter or two of the sediment surface (Fenchel and Straarup 1971). Therefore, although the artificial biofilms used in our experiments are not structurally representative of natural biofilms, we suggest that unless the true vertical Chl *a* distribution and the calibration function corresponding to this distribution are known, Chl *a* concentrations derived from the MPBI index must be reported under the assumption that the distribution is vertically homogeneous within the probing depth. One should bear in mind that if this assumption does not hold, the reported Chl *a* concentrations derived from the spectral-reflectance based measurements may be erroneous by up to 200% to 300% (see *Effects of vertical distribution of Chl* a). Clearly, this is a major limitation of the spectral reflectance-

based method with respect to absolute quantification of Chl *a* in sediments. On the other hand, this drawback can advantageously be used to monitor changes in the vertical Chl *a* distribution, e.g., due to vertical MPB migration, in a non-disruptive way and with a high spatial and temporal resolution. Moreover, if a two-layer distribution is an acceptable approximation for the description of the vertical Chl *a* distribution in the sediment, then quantification of the MPBI maxima and minima over the course of a day allows estimation of the migratory fraction of the Chl *a* standing stock (Fig. 8).

Third, the spectral reflectance-based method is unable to distinguish between Chl *a* and its degradation products in bulk natural sediments, as these have virtually identical absorption characteristics in the wavelength region used for the calculation of the MPB index (or any other spectral index used for MPB quantification in the literature). Therefore, hyperspectral imaging cannot replace methods, such as liquid chromatography, based on extraction and separation of the various Chl *a* forms, but can be used as a valuable supplement with benefits that the extraction-based methods lack (e.g., non-invasiveness) or can achieve only with an unreasonably large effort (high spatial resolution).

The hyperspectral imaging method presented here can provide useful insights in studies of microphytobenthos distribution and dynamics. Through its sub-millimeter spatial resolution, the method enables measurements of MPB distribution with an unprecedented level of detail and may thus alleviate the problem of chronic under-sampling of benthic habitats (Spilmont et al. 2011). By allowing minimally invasive in situ measurements of spatial and temporal patterns in the MPB distribution on a local scale, it allows studying mechanisms and processes by which they are regulated, such as physical forcing (Fig. 6A-C), bioturbation, and grazing (Fig. 6D-F), or diel variations in light (Fig. 8), which is required to improve our understanding of the ecological role and functions of MPB and its response to environmental changes (Miller et al. 1996; Seuront and Leterme 2006). Last but not least, it can bridge airborne remote sensing measurements with field-based ground-truthing, the latter traditionally done through sediment sampling, and thus enable critical analyses of patterns in benthic ecosystems that integrate effects from the scale of the organisms (microscale) to regional scales (Levin 1992; Chapman et al. 2010).

Comments and recommendations

Chlorophyll *a* quantification by the hyperspectral imaging method is based on the detection of spectral reflectance. Thus, measurements from a spectrally flat reference board are required to account for incident light spectrum and to convert the electronic signal measured by the imaging detector to reflectance. Ideally, these should be part of each scan, e.g., to account for possible changes in the spectrum of the incident light that may occur if scans are done at ambient illumination over extended periods of the day or during different days. If these changes are negligible, it is sufficient to scan the reference board separately and only once. The potential heterogeneity in the incident light intensity along the line-of-view detected by the imager, such as that occurring when artificial illumination by a lamp is used, are corrected for during data processing, where each captured spatial line in the scan is referenced against the corresponding (averaged) spatial line from the reference board (Bachar et al. 2008). In contrast, minor variability in the incident light intensity during the scan, such as that induced by a passing cloud when using ambient illumination, are automatically corrected for through the nature of the MPBI index, as long as the incident light field is similarly diffused and has the same shape of the spectrum. However, because this latter variability can be substantial, potentially leading to an over- or under-saturated signal by the imaging detector, it is recommended to conduct field measurements on a cloudless or overcast day, when such fluctuations are minimal.

Many of the spectral correction problems that are critical in hyperspectral imaging at remote-sensing scales are not relevant for imaging at the microscale. This is chiefly due to the comparatively short optical path length through the atmosphere. While this obviates the need for atmospheric corrections, albedo, etc, some attention has to be paid to the optical properties of the water column during field-based hyperspectral scans. Furthermore, microscale events that occur faster than the duration of scanning, such as lateral motion of the surficial sediment due to water flow, could be a source of spatial blurring or misinformation in the Chl *a* maps. Variations in the topography of the sediment surface could be larger than the depth of focus of the objective lens, leading to spectral mixing in neighboring points due to spatial blurring. This problem can be, however, minimized by using suitable optics with a longer depth of focus. Although not shown here, it is possible to use the grayscale imager to capture deformations of a laser line projected on the sediment surface to reconstruct the topography of the scanned sediment surface at a resolution similar to the hyperspectral image, in a similar manner as previously shown (Røy et al. 2005; Cook et al. 2007). This information could then be used to identify regions of the scanned area that are beyond the depth of focus and should therefore be excluded in subsequent analysis.

The spatial resolution of the hyperspectral maps is determined by the optical magnification of the objective, scanning speed of the line-of-view across the sediment, frame acquisition rate, and the imager-to-sediment distance. While these can be configured in several combinations, the resolution is ultimately limited by the intensity of the detected light and the sensitivity and signal-to-noise ratio of the imaging detector. The intensity of the back-scattered light can be increased by increasing the intensity of the incident irradiance, which can be achieved artificially, e.g., through lamps. However, to avoid potentially harmful effects of excessive light exposure, this additional illumination should not substantially exceed

the typical ambient intensities to which the studied biofilms are exposed. Artificial illumination is essential when measuring at night, i.e., when the ambient illumination is negligibly low. Under such circumstances, spectral imaging cannot be considered as a fully noninvasive technique, as the artificial illumination could trigger vertical migration in the MPB community. However, due to the rather brief duration of the measurement (10-15 min), our experience is that the artificial illumination will not have significant effects for that particular measurement. Whether or not it would cause significant migration that would be detectable in a subsequent measurement (e.g., in the next hour) is unknown and requires further investigation, although our results obtained during the last night of the vertical migration experiment (Fig. 8A) indicate that this is unlikely.

Owing to its modular design, the Hypersub system can be adapted for other applications than those presented in this report. For example, by attaching it to a submersible vehicle, the system can be used for rapid and more specific large-scale surveys of the sea-floor, e.g., in coral reef ecosystems, many of which are presently threatened by harmful microalgal colonization (McCook 2001). By adding a diver interface for viewing the imaged area and controlling the measurement, the system could be operated by a SCUBA diver in a similar interactive way as a regular underwater video recorder. Alternatively, by improving the water depth rating of the underwater housing, the system could be implemented as part of underwater observatories (Barnes et al. 2013) for long-term, remotely operated, or autonomous monitoring of the sea floor.

References

Al-Najjar, M. A. A., D. de Beer, M. Kühl, and L. Polerecky. 2012. Light utilization efficiency in photosynthetic microbial mats. Environ. Microbiol. 14:982-992 [doi:10.1111/j.1462-2920.2011.02676.x].

Azovsky, A., E. Chertoprood, M. A. Saburova, and I. G. Polikarpov. 2004. Spatio-temporal variability of micro- and meiobenthic communities in a White Sea intertidal sandflat. Estuar. Coast. Shelf Sci. 60:663-671 [doi:10.1016/j.ecss.2004.03.005].

Bachar, A., L. Polerecky, J. P. Fischer, K. Vamvakopoulos, D. de Beer, and H. M. Jonkers. 2008. Two-dimensional mapping of photopigment distribution and activity of Chloroflexus-like bacteria in a hypersaline microbial mat. FEMS Microbiol. Ecol. 65:434-448 [doi:10.1111/j.1574-6941.2008.00534.x].

Bale, A. J., and A. J. Kenny. 2007. Sediment analysis and seabed characterization, p. 43-86. *In* Methods for the study of marine benthos. Blackwell Science Ltd.

Barillé, L., J. -L. Mouget, V. Méléder, P. Rosa, and B. Jesus. 2011. Spectral response of benthic diatoms with different sediment backgrounds. Rem. Sens. Environ. 115:1034-1042 [doi:10.1016/j.rse.2010.12.008].

Barnes, C., M. Best, F. Johnson, L. Pautet, and B. Pirenne. 2013. Challenges, benefits, and opportunities in installing and operating cabled ocean observatories: Perspectives from NEPTUNE Canada. IEEE J. Ocean Eng. 38:144-157 [doi:10.1109/JOE.2012.2212751].

Bhaganagar, K., and T.-J. Hsu. 2009. Direct numerical simulations of flow over two-dimensional and three-dimensional ripples and implication to sediment transport: Steady flow. Coast. Eng. 56:320-331 [doi:10.1016/j.coastaleng.2008.09.010].

Brito, A., A. Newton, P. Tett, and T. Fernandes. 2009a. Development of an optimal methodology for the extraction of microphytobenthic chlorophyll. J. Int. Environ. Applic. Sci. 4:42-54.

———, ———, ———, and ———. 2009b. Temporal and spatial variability of microphytobenthos in a shallow lagoon: Ria Formosa (Portugal). Estuar. Coast. Shelf Sci. 83:67-76 [doi:10.1016/j.ecss.2009.03.023].

Carrère, V., N. Spilmont, and D. Davoult. 2004. Comparison of simple techniques for estimating chlorophyll a concentration in the intertidal zone using high spectral-resolution field-spectrometer data. Mar. Ecol. Prog. Ser. 274:31-40 [doi:10.3354/meps274031].

Chapman, M., T. Tolhurst, R. Murphy, and A. Underwood. 2010. Complex and inconsistent patterns of variation in benthos, micro-algae and sediment over multiple spatial scales. Mar. Ecol. Prog. Ser. 398:33-47 [doi:10.3354/meps08328].

Clark, R. N., and T. L. Roush. 1984. Reflectance spectroscopy: Quantitative analysis techniques for remote sensing applications. J. Geophys. Res. 89:6329 [doi:10.1029/JB089iB07p06329].

Consalvey, M., D. Paterson, and G. Underwood. 2004. The ups and downs of life in a benthic biofilm: migration of benthic diatoms. Diatom Res. 18:181-202 [doi:10.1080/0269249X.2004.9705870].

Cook, P. L. M., F. Wenzhöfer, R. N. Glud, F. Janssen, and M. Huettel. 2007. Benthic solute exchange and carbon mineralization in two shallow subtidal sandy sediments: Effect of advective porewater exchange. Limnol. Oceanogr. 52:1943-1963 [doi:10.4319/lo.2007.52.5.1943].

Farías, M. E., and others. 2013. The discovery of stromatolites developing at 3570 m above sea level in a high-altitude volcanic lake Socompa, Argentinean Andes. PloS One 8:e53497 [doi:10.1371/journal.pone.0053497].

Fenchel, T., and B. J. B. Straarup. 1971. Vertical distribution of photosynthetic pigments and the penetration of light in marine sediments. Oikos 22:172-182 [doi:10.2307/3543723].

Forster, R., and B. Jesus. 2006. Field spectroscopy of estuarine intertidal habitats. Int. J. Rem. Sens. 27:3657-3669 [doi:10.1080/01431160500500367].

Grinham, A. R., T. J. Carruthers, P. L. Fisher, J. W. Udy, and W. C. Dennison. 2007. Accurately measuring the abundance of

benthic microalgae in spatially variable habitats. Limnol. Oceanogr. Methods 5:119-125 [doi:10.4319/lom.2007.5.119].

Guarini, J., and G. Blanchard. 1998. Dynamics of spatial patterns of microphytobenthic biomass: inferences from a geostatistical analysis of two comprehensive surveys in Marennes-Oléron Bay (France). Mar. Ecol. Progr. Ser. 166:131-141 [doi:10.3354/meps166131].

Hakvoort, H., K. Heymann, C. Stein, and D. Murphy. 1997. In-situ optical measurements of sediment type and phytobenthos of tidal flats: a basis for imaging remote sensing spectroscopy. Ocean Dyn. 49:367-373.

Honeywill, C., D. Paterson, and S. Hagerthey. 2002. Determination of microphytobenthic biomass using pulse-amplitude modulated minimum fluorescence. Eur. J. Phycol. 37:485-492 [doi:10.1017/S0967026202003888].

Ionescu, D., and others. 2012. Microbial and chemical characterization of underwater fresh water springs in the Dead Sea. PloS One 7:e38319 [doi:10.1371/journal.pone.0038319].

Jesus, B., V. Brotas, M. Marani, and D. M. Paterson. 2005. Spatial dynamics of microphytobenthos determined by PAM fluorescence. Estuar. Coast. Shelf Sci. 65:30-42 [doi:10.1016/j.ecss.2005.05.005].

———, R. Perkins, and C. Mendes. 2006. Chlorophyll fluorescence as a proxy for microphytobenthic biomass: alternatives to the current methodology. Mar. Biol. 150:17-28 [doi:10.1007/s00227-006-0324-2].

Joint, I., J. Gee, and R. Warwick. 1982. Determination of fine-scale vertical distribution of microbes and meiofauna in an intertidal sediment. Mar. Biol. 72:157-164 [doi:10.1007/BF00396916].

Kazemipour, F., V. Méléder, and P. Launeau. 2011. Optical properties of microphytobenthic biofilms (MPBOM): Biomass retrieval implication. J. Quant. Spectrosc. Radiative Trans. 112:131-142 [doi:10.1016/j.jqsrt.2010.08.029].

Kohls, K., R. M. M. Abed, L. Polerecky, M. Weber, and D. de Beer. 2010. Halotaxis of cyanobacteria in an intertidal hypersaline microbial mat. Environ. Microbiol. 12:567-75 [doi:10.1111/j.1462-2920.2009.02095.x].

Kokaly, R. F., and R. N. Clark. 1999. Spectroscopic determination of leaf biochemistry using band-depth analysis of absorption features and stepwise multiple linear regression. Rem. Sens. Environ. 67:267-287 [doi:10.1016/S0034-4257(98)00084-4].

Krause-Jensen, D., and K. Sand-Jensen. 1998. Light attenuation and photosynthesis of aquatic plant communities. Limnol. Oceanogr. 43:396-407 [doi:10.4319/lo.1998.43.3.0396].

Kromkamp, J. C., E. P. Morris, R. M. Forster, C. Honeywill, S. Hagerthey, and D. M. Paterson. 2006. Relationship of intertidal surface sediment chlorophyll concentration to hyperspectral reflectance and chlorophyll fluorescence. Estuaries and Coasts 29:183–196.

Kühl, M., and B. B. Jørgensen. 1994. The light field of microbenthic communities: radiance distribution and microscale optics of sandy coastal sediments. Limnol. Oceanogr. 39:1368-1398 [doi:10.4319/lo.1994.39.6.1368].

———, C. Lassen, and B. B. Jørgensen. 1994. Light penetration and light intensity in sandy marine sediments measured with irradiance and scalar irradiance fiberoptic microprobes Rid A-1977-2009. Mar. Ecol. Progr. Ser. 1:139-148 [doi:10.3354/meps105139].

———, and L. Polerecky. 2008. Functional and structural imaging of phototrophic microbial communities and symbioses. Aquat. Microb. Ecol. 53:99-118 [doi:10.3354/ame01224].

Lassen, C., H. Ploug, and B. B. Jørgensen. 1992. Microalgal photosynthesis and spectral scalar irradiance in coastal marine sediments of Limfjorden, Denmark. Limnol. Oceanogr. 37:760-772 [doi:10.4319/lo.1992.37.4.0760].

Levin, S. 1992. The problem of pattern and scale in ecology: the Robert H. MacArthur award lecture. Ecology 73:1943-1967 [doi:10.2307/1941447].

Lorenzen, C. 1967. Determination of chlorophyll and pheopigments: spectrophotometric equations. Limnol. Oceanogr. 12:343-346 [doi:10.4319/lo.1967.12.2.0343].

MacIntyre, H., R. Geider, and D. Miller. 1996. Microphytobenthos: The ecological role of the "secret garden" of unvegetated, shallow-water marine habitats. I. Distribution, abundance and primary production. Estuar. Coasts 19:186-201 [doi:10.2307/1352224].

McCook, L. J. 2001. Competition between corals and algal turfs along a gradient of terrestrial influence in the nearshore central Great Barrier Reef. Coral Reefs 19:419-425.

Miller, D., R. Geider, and H. MacIntyre. 1996. Microphytobenthos: the ecological role of the "secret garden" of unvegetated, shallow-water marine habitats. II. Role in sediment stability and shallow-water food webs. Estuaries Coasts 19:202-212 [doi:10.2307/1352225].

Mitbavkar, S., and A. C. Anil. 2004. Vertical migratory rhythms of benthic diatoms in a tropical intertidal sand flat: influence of irradiance and tides. Mar. Biol. 145:9-20 [doi:10.1007/s00227-004-1300-3].

Montagna, P., G. Blanchard, and A. Dinet. 1995. Effect of production and biomass of intertidal microphytobenthos on meiofaunal grazing rates. J. Exp. Mar. Biol. Ecol. 185:149-165 [doi:10.1016/0022-0981(94)00138-4].

Moreno, S., and F. X. Niell. 2004. Scales of variability in the sediment chlorophyll content of the shallow Palmones River Estuary, Spain. Estuar. Coast. Shelf Sci. 60:49-57 [doi:10.1016/j.ecss.2003.06.006].

Murphy, R. J., T. J. Tolhurst, M. G. Chapman, and A. J. Underwood. 2004. Estimation of surface chlorophyll on an exposed mudflat using digital colour-infrared (CIR) photography. Estuar. Coast. Shelf Sci. 59:625-638 [doi:10.1016/j.ecss.2003.11.006].

———, T. J. Tolhurst, M. G. Chapman, and A. J. Underwood.

2005. Estimation of surface chlorophyll-a on an emersed mudflat using field spectrometry: accuracy of ratios and derivative-based approaches. Int. J. Rem. Sens. 26:1835-1859 [doi:10.1080/01431160512331326530].

———, ———, ———, and ———. 2008. Spatial variation of chlorophyll on estuarine mudflats determined by field-based remote sensing. Mar. Ecol. Progr. Ser. 365:45-55 [doi:10.3354/meps07456].

———, A. J. Underwood, and A. C. Jackson. 2009. Field-based remote sensing of intertidal epilithic chlorophyll: Techniques using specialized and conventional digital cameras. J. Exp. Mar. Biol. Ecol. 380:68-76 [doi:10.1016/j.jembe.2009.09.002].

Nozais, C., R. Perissinotto, and S. Mundree. 2001. Annual cycle of microalgal biomass in a South African temporarily-open estuary: nutrient versus light limitation. Mar. Ecol. Progr. Ser. 223:39-48 [doi:10.3354/meps223039].

Palmer, J. D., and F. E. Round. 1967. Persistent, vertical-migration rhythms in benthic microflora. VI. The tidal and diurnal nature of the rhythm in the diatom Hantzschia virgata. Biol. Bull. 132:44-55 [doi:10.2307/1539877].

Polerecky, L., and others 2009a. Modular spectral imaging system for discrimination of pigments in cells and microbial communities. Appl. Environ. Microbiol. 75:758-771 [doi:10.1128/AEM.00819-08].

———, J. M. Klatt, M. A. A. Al-Najjar, and D. de Beer. 2009b. Hyper-spectral imaging of biofilm growth dynamics. Hyperspectral Image Signal Processing: Evolution in Remote Sensing. WHISPERS '09. 1-4.

Rasmussen, A., G. Banta, and O. Andersen. 1998. Effects of bioturbation by the lugworm Arenicola marina on cadmium uptake and distribution in sandy sediments. Mar. Ecol. Progr. Ser. 164:179-188 [doi:10.3354/meps164179].

Røy, H., M. Huettel, and B. B. Jørgensen. 2005. The influence of topography on the functional exchange surface of marine soft sediments, assessed from sediment topography measured in situ. Limnol. Oceanogr. 50:106-112 [doi:10.4319/lo.2005.50.1.0106].

Serôdio, J., J. Marques da Silva, and F. Catarino. 1997. Nondestructive tracing of migratory rhythms of intertidal benthic microalgae using in vivo chlorophyll a fluorescence. J. Phycol. 33:542-553 [doi:10.1111/j.0022-3646.1997.00542.x].

Seuront, L., and N. Spilmont. 2002. Self-organized criticality in intertidal microphytobenthos patch patterns. Physica A: Stat. Mech. Applic. 313:513-539 [doi:10.1016/S0378-4371(02)00989-5].

———, and S. Leterme. 2006. Microscale patchiness in microphytobenthos distributions: evidence for a critical state, p. 167-186. *In* J. C. Kromkamp, J. De Brouwer, G. F. Blanchard, R. M. Forster, and V. Créach [eds.], Functioning of microphytobenthos in estuaries. Publisher: Royal Netherlands Academy of Arts and Sciences.

Spilmont, N., D. Davoult, and A. Migné. 2006. Benthic primary production during emersion: In situ measurements and potential primary production in the Seine Estuary (English Channel, France). Mar. Poll. Bull. 53:49-55 [doi:10.1016/j.marpolbul.2005.09.016].

———, L. Seuront, T. Meziane, and D. T. Welsh. 2011. There's more to the picture than meets the eye: Sampling microphytobenthos in a heterogeneous environment. Estuar. Coast. Shelf Sci. 95:470-476 [doi:10.1016/j.ecss.2011.10.021].

Stal, L. 2010. Microphytobenthos as a biogeomorphological force in intertidal sediment stabilization. Ecol. Eng 36:236-245 [doi:10.1016/j.ecoleng.2008.12.032].

Sundbäck, K., V. Enoksson, W. Graneli, and K. Pettersson. 1991. Influence of sublittoral microphytobenthos on the oxygen and nutrient flux between sediment and water: a laboratory continuous-flow study. Mar. Ecol. Progr. Ser. 74:263-279 [doi:10.3354/meps074263].

Underwood, A. J., M. G. Chapman, and S. D. Connell. 2000. Observations in ecology: you can't make progress on processes without understanding the patterns. J. Exp. Mar. Biol. Ecol. 250:97-115 [doi:10.1016/S0022-0981(00)00181-7].

Volkenborn, N., L. Polerecky, D. S. Wethey, and S. A. Woodin. 2010. Oscillatory porewater bioadvection in marine sediments induced by hydraulic activities of Arenicola marina. Limnol. Oceanogr. 55:1231-1247 [doi:10.4319/lo.2010.55.3.1231].

Whitney, D., and W. Darley. 1979. A method for the determination of chlorophyll *a* in samples containing degradation products. Limnol. Oceanogr. 24:183-186 [doi:10.4319/lo.1979.24.1.0183].

Yang, L., and S. J. Miklavcic. 2005. Revised Kubelka-Munk theory. III. A general theory of light propagation in scattering and absorptive media. J. Optic. Soc. Amer. A 22:1866 [doi:10.1364/JOSAA.22.001866].

Submitted 19 April 2013
Revised 6 September 2013
Accepted 17 September 2013